Evaporation-Driven 3D CNT Scaffolding

for Composite Reinforcement

A. Nissenbaum*, I. Greenfeld* and H.D. Wagner
Department of Materials & Interfaces, Weizmann Institute of Science
Rehovot 76100, Israel

*These authors contributed equally to this work

Supplementary material

S1. Calibration of CNT suspension via UV-vis

The calibration was conducted using UV-vis spectroscopy at a low-concentration range. The calibration was carried out at λ=270nm peak, which is less affected by variation in the CNT concentration. The scan was carried out at absorbance mode with wavelength in the range of 200-800nm. See Figure S1.
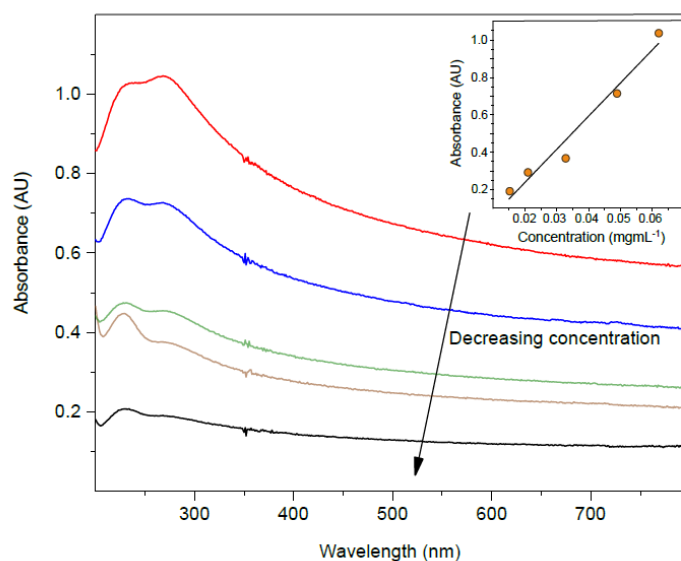

Figure S1: **Calibration curve for CNT solution concentration measurements.** UV-vis spectra of several low-concentration CNT/SDS solutions. The inset calibration graph was used to determine the solution extinction coefficient.

S2. Evaporation-driven self-assembly (EDSA)

S2.1. EDSA concept and experimental

Self-assembly of particles can occur spontaneously if the particles are strongly attracted to each other and/or if the environmental conditions drive the particles to phase-separate from mixed to assembled state. In general, CNTs have strong affinity to each other and can only be homogeneously dispersed using surfactants, mechanical shear mixing, or functionalization[1], which can overcome the attraction forces and maintain a homogenously dispersed state. Consequently, the driving force for assembly should be primarily environmental.

In EDSA, the assembly of particles is initiated and dictated by an evaporation gradient that occurs when a contained liquid is left to evaporate. The evaporation gradient is the result of the varying evaporation flux along the liquid curved profile. Deegan et al[2] published a theoretical and experimental analysis of the well-known "coffee-ring" effect, a special case of evaporation-induced deposition. Although they describe a sessile drop on a surface, the broad concept of evaporation-induced assembly is universal. In a contained liquid with an immersed solid substrate, the contact line (the line that meets all phases) is provisionally anchored to the solid surface, such that when the liquid is evaporating, the contact area is not diminished. In addition, the evaporation flux close to the contact line is larger than the flux elsewhere. To maintain the pinned contact line, liquid is driven toward the contact line to compensate for the excessive evaporation in that region.

If particles are dispersed in the liquid, they are carried with it, and once they reach the contact line and the liquid evaporates, they are deposited on the solid surface. Since in an open environment evaporation continues until the entire liquid volume is depleted, the feed of particles toward the contact line is continuous. This mechanism, clearly visual in any coffee stain, causes a thick yet homogenous deposition of particles at the contact line. The deposition shape and pattern depend on the geometry and orientation of the substrate, as well as on the surface tension and evaporation rate of the liquid. Since EDSA invokes a physical mechanism that depends only on evaporation, it can theoretically deposit any type of particles as long as their dispersion in the solution is fairly homogeneous.

Due to these unique deposition characteristics, EDSA is an attractive method for depositing particles or nanoparticles such as CNTs on solid surfaces[3,4]. It was observed that when EDSA is performed over a flat smooth surface, a stick-slip mechanism of the contact line results in an intermittent stripe deposition[5–7]. For example, Shastry et al[8] have used EDSA to

deposit several types of CNTs on ceramic surfaces. The surfaces were coated with even, thick stripes of CNTs, where intermittent deposition was strongly evident. Similar results can be found in the work of Xiao et al[9]. Although the EDSA method proved to be efficient and easy for nanoparticle deposition, it was mainly conducted on planar solid surfaces, whereas other types of solid geometries such as microfibers were left aside. However, microfibers were CNT-coated by related methods such as dip-coating, where a fiber is dipped and pulled out of a nanoparticles-rich suspension. Although the methods are similar in methodology, the mechanism of deposition in dip-coating is by no means similar to EDSA, as the former relies on local grafting of the nano particles to the fiber substrate, neglecting the kinetic and thermodynamic processes that are fundamental to EDSA.

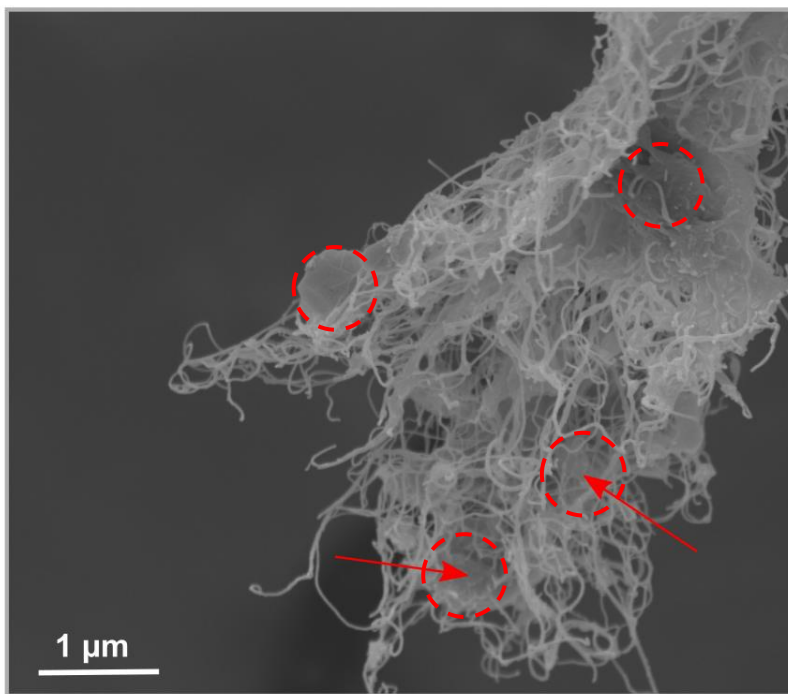## S2.2. SDS and CNT interaction during EDSA

Figure S2: Crystallized SDS platelets in the CNT scaffold. High magnification SEM micrograph displays microscale SDS platelets where individual CNTs are randomly fused within (examples are circled).

S3. Pore diameter estimation using ImageJ

The average pore diameter of the CNT scaffold was estimated using SEM image analysis through ImageJ built-in particle size feature (Figure S3).
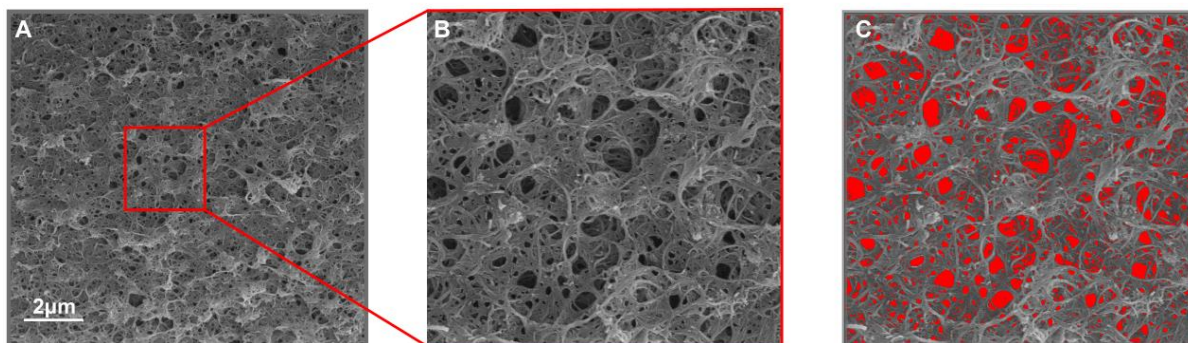

Figure S3: **Pore analysis process using ImageJ particle size feature. A** –Selected SEM micrograph of the scaffold porous surface. Typical area of interest (AOI) is marked by the red rectangle. **B** –Magnified AOI micrograph. **C** – Threshold process to distinguish the scaffold pores. The pores are highlighted in red.

We find this approach preferable over other methods such as µCT segmentation because of the high contrast of CNT/pores and the ultrahigh resolution that is provided by SEM. These elements minimize the human bias when thresholding an image. The analysis was carried out by selecting several areas of interest (AOIs) from relatively low SEM magnification (Figure S3A). The AOIs were then magnified at about X2 (Figure S3B) and image threshold was applied on the AOIs (Figure S3C). We note that since SEM images have a certain visible depth (that is, several layers of nanotubes appear in the image) we applied a threshold of $600nm^2$ pore area and pore circularity threshold of 0.8, to avoid misreading small voids that arise from the intersection between each CNT layer as pores.

S4. Finite element analysis of the evaporation power slope

The evaporation flux varies as a function of the vertical downward distance from the meniscus tip (Figure 2A in the manuscript). The flux dependence on the distance x can be approximated by a power relation, given by

$$J = J_0 \left(\frac{x}{h}\right)^{-\lambda} \tag{1}$$

where J_0 is the evaporation flux of still water, h is the meniscus height, and the exponent λ is dependent on the meniscus shape. λ can be obtained by solving the equivalent problem of an electrostatic potential field, where the vapor concentration is equivalent to the potential, and the evaporation flux is equivalent to the electric field. Both vapor concentration and electrostatic potential obey the Laplace equation for a potential field, $\nabla^2 \phi = 0$, where ϕ is a scalar independent variable which can be electrostatic potential, temperature, concentration, etc. The potential gradient, $\nabla \phi$, is the electric field in the case of an electrostatic field, or the evaporation flux in the case of evaporation.

The estimation of λ for the catenary shape was done by finite element analysis (Figure S4). The power slope of the electric field along the catenary was obtained by curve fitting ($R^2 > 0.99$) of the field magnitude along the catenary, for several values of the contact angle θ_c. For the geometry of our EDSA experiment and a zero contact angle, the exponent obtained is $\lambda(\theta_c = 0) \cong 0.41$. By comparison, the same analysis carried out for the meniscus of a flat vertical wall yielded $\lambda(\theta_c = 0) \cong 0.55$, representing an infinitely large fiber radius. The exponent for a spherical drop on a flat surface is $\lambda(\theta_c = 0) \cong 0.5$.
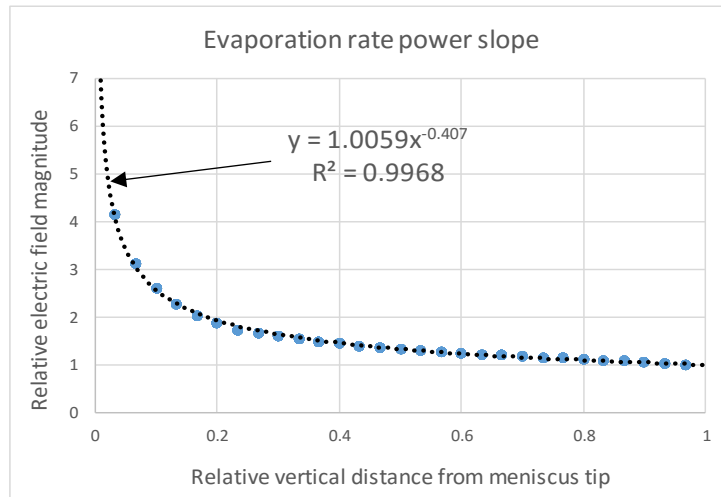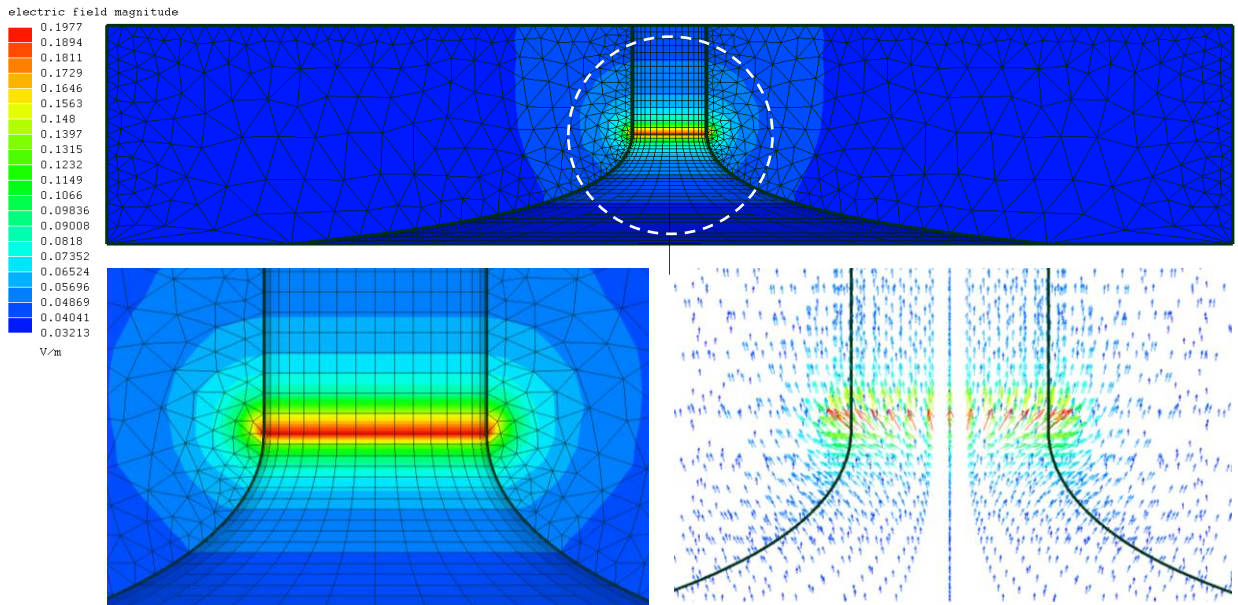
Figure S4: 3D Finite element simulation around the meniscus. Example for $\theta_c = 0$. The electric field propagates in air (the solid body), and is analogous to the evaporation rate. The boundary potentials are 1V at the bottom and 0.8V at the top. The top image shows the variation of the field magnitude along the catenary shape. The mid images show magnification of the field magnitude and the vector field. The bottom plot presents the fit of the field magnitude to a power function of the vertical distance from the meniscus tip.

S5. Adhesion between CNTs and the fiber

Since the quartz fiber and CNTs are not functionalized, the adsorption of CNTs on the quartz fiber surface is through surface friction and weak attraction forces. When pulling-out the fiber from the scaffold before impregnation by the epoxy matrix, full debonding is observed (Figure S5.1A). Furthermore, the surface of the quartz fiber remains partially coated with a few layers of CNTs (Figure S5.1B and D), implying that the adhesion strength is comparable to the strength of the un-impregnated scaffold. The strength of the CNTs network is essentially low because the CNTs are only entangled loosely, and are easily disentangled (Figure S5.1C) and drawn approximately to their full length. Therefore, we assess that the interfacial strength prior to impregnation is negligible.
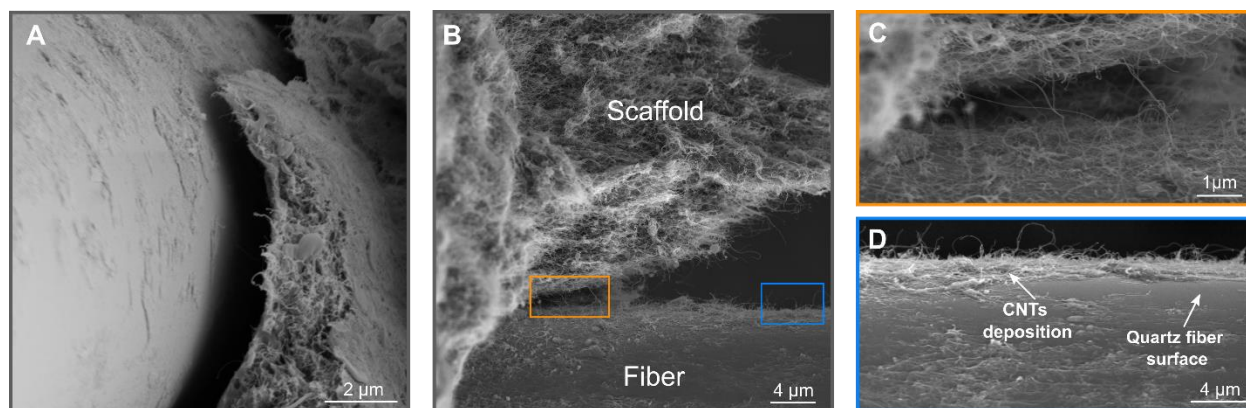

Figure S5.1: Un-impregnated CNT-scaffold/quartz fiber. A - A top view SEM image of an un-impregnated assembly of quartz fiber and CNT scaffold displays complete debonding between the scaffold and the fiber. **B** – The interface region between the scaffold and the fiber. **C** – A magnified view of the interface debonding region. The interface separation displays disentanglement of CNT from the surface of the fiber. **D** - A magnification of the fiber surface displays a pilled-off coating from the quartz surface, and large portions of the quartz surface are uncoated.

During fracture of the impregnated scaffold, a small portion of the CNTs pull out from the matrix whereas the majority of CNTs break, as seen in Figure S5.2.
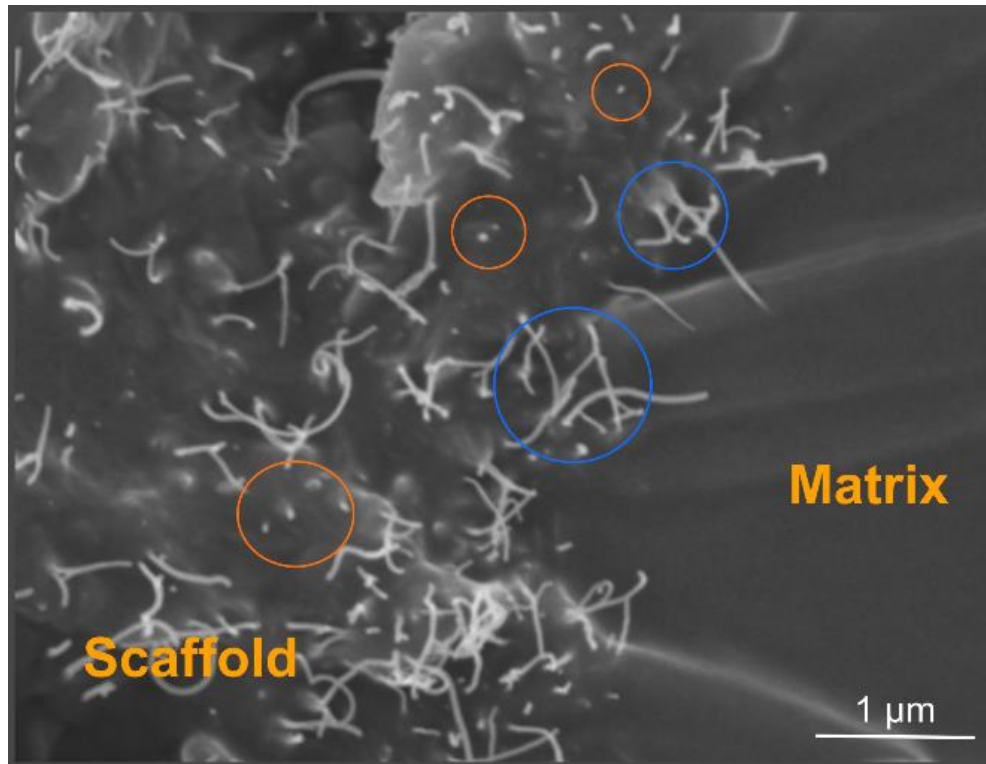

Figure S5.4: The fracture surface of CNT scaffold/matrix composite. SEM image of the fracture surface. The orange circles display CNTs that broke approximately at the fracture surface. The blue circles display CNTs that were pulled out.

S6. Finite element analysis of the fiber-scaffold-matrix composite

The purpose of this analysis is to assess the effect of the quartz fiber on the mechanical properties of the entire composite assembly, including the fiber, impregnated scaffold, and matrix. The analysis demonstrates that the fiber contribution can be neglected (Figure S5).
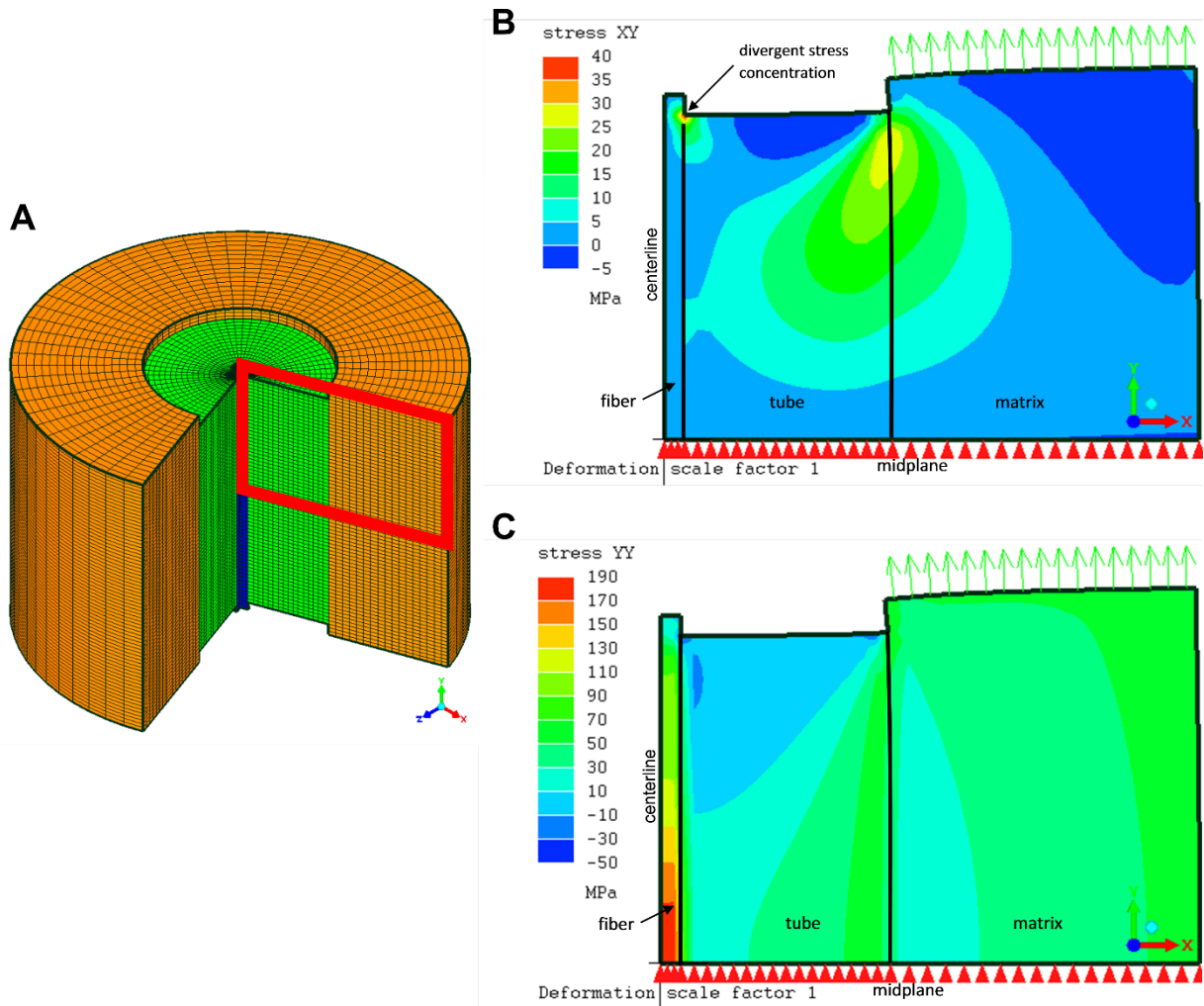

Figure S6: Stresses in the fiber-scaffold-matrix composite. A – Axisymmetric model for finite element analysis (FEA), with y-axis as the centerline and x-axis as the radial dimension. The red frame indicates the region of the stress maps presented in B and C. **B** – Shear stress in a fragment of critical aspect, $\ell_F/D_t = 1.41$. A divergent shear stress concentration is indicated at the top corner of the fiber-tube interface, a likely nucleus for a debonding crack. **C** - Tensile stress in a fragment of critical aspect. The fiber contribution to the tensile load carried by the tube and fiber assembly at the midplane is 3.7%. The tube internal diameter is $D_f = 9$ μm and its external diameter is $D_t = 50$ μm. The load is a uniform tensile stress of 50 MPa on the upper face of the matrix, and the midplane is constrained in the y-direction. The matrix, tube and fiber elastic moduli used in the model are 1 MPa, 5 MPa and 80 MPa, respectively.

S7. Analysis of the scaffold strength dependence on CNT length

Long CNTs are semi flexible and tend to coil into random conformations (Figure 1C in the main text). Hence, a CNT can be described as a self-avoiding random walk (SAW) of many rigid segments[10–12], in a similar way to a polymer chain in solution[13]. This leads to a power law for the end-to-end distance of a CNT, $R \propto (l^{CNT})^{\nu}$, where the exponent $\nu \cong 0.588$ is the inverse of the fractal dimension of an SAW object at 3D[13]. During EDSA, when the CNTs are deposited on the fiber, their occupying volumes, $\sim R^3$, start to overlap. The corresponding overlap volume concentration scales as the ratio between the contour volume of a CNT, proportional to l^{CNT}, and the occupying volume:

$$\phi^* \propto \frac{l^{CNT}}{R^3} \propto (l^{CNT})^{1-3\nu} \propto (l^{CNT})^{-0.76} \tag{2}$$

The occupying volumes of neighboring CNTs penetrate each other, causing the CNTs to entangle and create a network. The corresponding entanglement concentration, $\phi_e \propto (l^{CNT})^{-0.76}$, scales the same as ϕ^* but with a larger constant prefactor (not shown). This concentration can serve as the scale for the CNTs volume fraction in the scaffold, so that

$$V_c = k(l^{CNT})^{-0.76} \tag{3}$$

where k is a constant prefactor. k itself may vary with respect to the CNT degree of flexibility, which is inversely related to the persistence length[10]. The CNT becomes more flexible when its bending stiffness EI is lower[12], resulting in tighter and smaller CNT coils and therefore higher V_c.

Given the same CNT type and diameter as in our experiments, the prefactor can be fitted using the CNT's volume fraction $V_c = 0.2$ and average length $l^{CNT} = 12.5$ μm, yielding $k = V_c(l^{CNT})^{0.76} = 1.38$ μm$^{0.76}$. The maximum possible CNT volume fraction is $V_c^{\max} = 1 - V_s$, occurring when the CNTs are tightly packed together with the surfactant, leaving no space for the matrix. However, practically, the epoxy matrix would infiltrate into the scaffold by capillarity[14], so that stress transfer from the matrix to the CNTs will be upheld even with a small amount of matrix. The matching CNT length at $V_c^{\max}$, given $V_s = 0.2$, is $l_e^{CNT} = 2.04$ μm (Equation (3)), denoted l_e^{CNT} to mark the entanglement threshold; shorter CNTs will not entangle because V_c cannot be increased further, and consequently the CNT coils will cease to overlap.

Substituting the expression of V_c from Equation (3) into the composite strength expression (Equation (9) in the main text), we obtain a prediction for the strength as a function of the CNT average length:

$$\sigma_t = \frac{1}{5}\left(1 - \frac{1}{4}\frac{\sigma_c D_{CNT}}{\tau_i l^{CNT}}\right)k(l^{CNT})^{-0.76}\sigma_c$$
$$+ (1 - V_s - k(l^{CNT})^{-0.76})\sigma_m \tag{4}$$

Note that ℓ_c^{CNT} was inserted explicitly, to show the detailed dependencies, and that V_m was replaced by the volume fraction left after removing the surfactant and CNT volume fractions. V_c and σ_t (Equations (3) and (4), respectively) are depicted in Figure 6 in the main text as functions of l^{CNT}, with all other parameters as in our experiment. Both functions rise sharply when the CNT length is reduced, until a maximum possible V_c is reached. Although the length factor η_l (left parenthesis in Equation (4)) gradually decreases when the CNT length is reduced, the scaffold composite strength keeps increasing because of the rising CNT volume fraction. Below the minimum value for entanglement, l_e^{CNT}, the CNTs will not form an entangled network, but rather short, tightly packed bundles[12]; in this region, the composite strength decreases sharply, as η_l decreases while V_c remains constant. Below the CNT critical length, ℓ_c^{CNT}, the composite strength further degrades because the short CNTs tend to pull out instead of break (in this region, the length factor changes to $\eta_l = l^{CNT}/2\ell_c^{CNT}$)[15]. Note that, in Equation (4), the term $\sigma_c D_{CNT} \sim (4t/D_{CNT})D_{CNT} \sim t$ so that η_l is not dependent on the CNT diameter but instead on its wall thickness, which is constant (graphene layer thickness).

References

[1]   L. Vaisman, H.D. Wagner, G. Marom, The role of surfactants in dispersion of carbon nanotubes, Adv. Colloid Interface Sci. 128–130 (2006) 37–46. https://doi.org/10.1016/j.cis.2006.11.007.

[2]   R.D. Deegan, O. Bakajin, T.F. Dupont, G. Huber, S.R. Nagel, T. a Witten, Capillary flow as the cause of ring stains from dried liquid drops, Lett. to Nat. 389 (1997) 827–829. https://doi.org/10.1038/39827.

[3]   A. Shimoni, S. Azoubel, S. Magdassi, Inkjet printing of flexible high-performance carbon nanotube transparent conductive films by "coffee ring effect"., Nanoscale. 6 (2014) 11084–9. https://doi.org/10.1039/c4nr02133a.

[4]   Y. Tai, G. Lubineau, Heating-Rate-Triggered Carbon-Nanotube-based 3-Dimensional Conducting Networks for a Highly Sensitive Noncontact Sensing Device, Sci. Rep. 6 (2016) 19632.

https://doi.org/10.1038/srep19632.

[5]   M.E.R. Shanahan, Simple Theory of Stick-Slip Wetting Hysteresis, Langmuir. 11 (1995) 1041–1043. https://doi.org/Doi 10.1021/La00003a057.

[6]   M. Shanahan, K. Sefiane, Kinetics of triple line motion during evaporation, Contact Angle, Wettability …. (2009) 1–25. https://doi.org/10.1163/ej.9789004169326.i-400.12.

[7]   J.F. Joanny, P.G. de Gennes, A model for contact angle hysteresis, J. Chem. Phys. 81 (1984) 552. https://doi.org/10.1063/1.447337.

[8]   T.A. Shastry, J.-W.T. Seo, J.J. Lopez, H.N. Arnold, J.Z. Kelter, V.K. Sangwan, L.J. Lauhon, T.J. Marks, M.C. Hersam, Large-Area, Electronically Monodisperse, Aligned Single-Walled Carbon Nanotube Thin Films Fabricated by Evaporation-Driven Self-Assembly, Small. 9 (2013) 45–51. https://doi.org/10.1002/smll.201201398.

[9]   L. Xiao, J. Wei, Y. Gao, D. Yang, H. Li, Formation of gradient multiwalled carbon nanotube stripe patterns by using evaporation-induced self-assembly, ACS Appl. Mater. Interfaces. 4 (2012) 3811–3817. https://doi.org/10.1021/am300936a.

[10]   H.S. Lee, C.H. Yun, H.M. Kim, C.J. Lee, Persistence length of multiwalled carbon nanotubes with static bending, J. Phys. Chem. C. 111 (2007) 18882–18887. https://doi.org/10.1021/jp075062r.

[11]   F. Schütt, S. Signetti, H. Krüger, S. Röder, D. Smazna, S. Kaps, S.N. Gorb, Y.K. Mishra, N.M. Pugno, R. Adelung, Hierarchical self-entangled carbon nanotube tube networks, Nat. Commun. 8 (2017) 1–10. https://doi.org/10.1038/s41467-017-01324-7.

[12]   Z. Shen, M. Roding, M. Kroger, Y. Li, Carbon nanotube length governs the viscoelasticity and permeability of buckypaper, Polymers (Basel). 9 (2017) 1–18. https://doi.org/10.3390/polym9040115.

[13]   M. Rubinstein, R.H. Colby, Polymer Physics, Oxford University Press, 2003.

[14]   X.M. Sui, I. Greenfeld, H. Cohen, X.H. Zhang, Q.W. Li, H.D. Wagner, Multilevel composite using carbon nanotube fibers (CNTF), Compos. Sci. Technol. 137 (2016) 35–43. https://doi.org/10.1016/j.compscitech.2016.10.011.

[15]   I. Greenfeld, H.D. Wagner, Nanocomposite toughness, strength and stiffness: role of filler geometry, Nanocomposites. 1 (2015) 3–17. https://doi.org/10.1179/2055033214Y.0000000002.